Heat-mode excitation in a proximity superconductor

A.O. Denisov,^{1,2} A.V. Bubis,^{3,1} S.U. Piatrusha,¹ N.A. Titova,⁴ A.G. Nasibulin,^{3,5} J. Becker,⁶ J. Treu,⁶ D. Ruhstorfer,⁶ G. Koblmüller,⁶ E.S. Tikhonov,¹ and V.S. Khrapai¹

¹ Institute of Solid State Physics, Russian Academy of Sciences, 142432 Chernogolovka, Russian Federation
 ² Department of Physics, Princeton University, Princeton, New Jersey 08544, USA
 ³ Skolkovo Institute of Science and Technology, Nobel street 3, 121205 Moscow, Russian Federation
 ⁴ Moscow State University of Education, 29 Malaya Pirogovskaya St, Moscow, 119435, Russia
 ⁵ Aalto University, P. O. Box 16100, 00076 Aalto, Finland
 ⁶ Walter Schottky Institut, Physik Department, and Center for Nanotechnology and Nanomaterials, Technische Universität München, Am Coulombwall 4, Garching 85748, Germany

Mesoscopic superconductivity deals with various excitation modes, only one of them – the charge-mode – being directly accessible for conductance measurements due to the imbalance in populations of quasi-electron and quasi-hole excitation branches. Other modes carrying heat or even spin, valley etc. currents are much harder to control for their charge-neutral origin. This noticeable gap in the experimental studies of mesoscopic non-equilibrium superconductivity can be filled by going beyond the conventional DC transport measurements and exploiting spontaneous current fluctuations. Here, we perform the first experiment of this kind and investigate the transport of heat in an open hybrid device based on a superconductor proximitized InAs nanowire. Using shot noise measurements we observe a novel effect of Andreev heat transmission along the superconducting interface and fully characterize it in terms of the thermal conductance on the order of $G_{\rm th} \sim e^2/h$, tunable by a back gate voltage. Understanding of the heat-mode also uncovers its implicit signatures in the non-local charge transport. Our experiments open a direct pathway to probe generic neutral excitations in superconducting hybrids.

Conversion of a quasiparticle current to the collective motion of a Cooper pair condensate at the interface of a normal metal and superconductor is known as Andreev reflection (AR)¹. For quasiparticle energies below the superconducting gap (sub-gap quasiparticles) AR is fully responsible for the charge transport across the interface. Conservation of both the number of sub-gap quasiparticles and their excitation energy on the normal side manifests AR as a fundamental example of charge-heat separation in the electronic system. While heat transport transverse to the interface is blocked by the AR, it does not vanish in the direction along the superconductor. In this way, ARs mediate the heat conduction via vortex core in s-type superconductors² and via neutral modes in graphene³.

The retro-character of the AR, that is the propagation of a reflected hole via the time-reversed trajectory of an incident electron, results in a suppression of the heat conductance in the ballistic limit. This obstacle may be overcome by imposing the chirality of the charge carriers in a magnetic field^{4,5}, similar to quantum Hall based experiments⁶, or by going in the regime of specular AR near charge-neutrality point in graphene⁷. In the diffusive limit, counter-intuitively, the heat transport is restored, since moderate disorder scattering effectively increases the number of the conducting modes⁸. Furthermore, by increasing the number of ARs disorder scattering can promote the relaxation of the charge-mode non-equilibrium in favor of the heat-mode, similar to the case of anisotropic superconductors⁹. All of this makes the geometry of the Andreev wire⁸ – a diffusive normal core proximitized by a wrapped around superconductor - preferable for a sub-gap heat transport experiment.

In this work we challenge a thermal conductance (G_{th}) measurement in an open three-terminal hybrid device based on a diffusive InAs nanowire (NW) proximitized by a superconducting contact, see the image of one of our samples in Fig. 1a. Conceptually similar devices were investigated in the context of Cooper-pair splitters 10-12 and, more recently, Majorana physics 13-17 with the emphasis on the electric conductance. The central part of the device represents a few 100 nm long Andreev wire with a partial superconducting wrap, that removes complications arising from the Little-Parks effect 18,19. Using shot noise measurements we identify the heat transport carried by the sub-gap states in the NW, as well as its implications for the non-local charge transport. Our experiments offer a so far missing experimental tool in the field of non-equilibrium mesoscopic superconductivity^{20–25} and enable the control of generic charge-neutral excitations in superconducting hybrids.

The outline of our experiment is depicted in Fig. 1b. A semiconducting InAs nanowire is equipped with a superconducting (S) terminal, made of Al, in the middle and two normal metal (N) terminals, made of Ti/Au bilayer, on the sides. In essence, this device represents two backto-back normal metal-NW-superconductor (NS) junctions sharing the same S terminal. Note the absence of the quantum $dots^{10,12,16}$ or tunnel barriers¹⁵ adjacent to the S-terminal, that enables better coupling of the subgap states to the normal conducting regions. Throughout the experiment the S terminal is grounded, terminal N1 is biased and terminal N2 is floating (or vice versa). The S terminal serves as a nearly perfect sink for the charge current I_1 , which is driven in a biased NS junction via the terminal N1. At energies below the superconducting

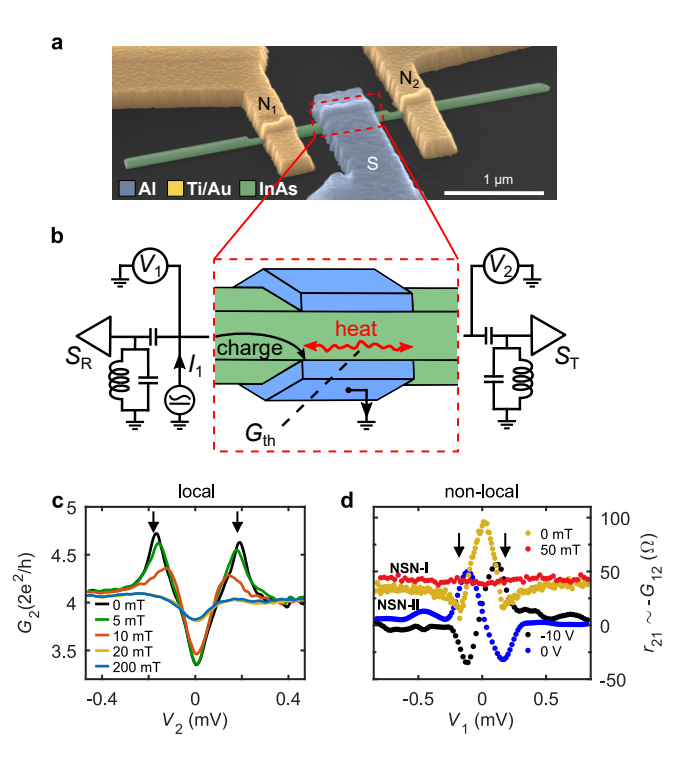


FIG. 1. Outline and charge transport data. (a) Scanning electron microscope image of the typical device (false color). InAs NW is equipped with two N terminals (Ti/Au) on the sides and one S terminal (Al) in the middle. (b) Separation of charge and heat currents at the InAs/Al interface. Three-terminal configuration allows studying thermal conductance $G_{\rm th}$ of the proximitized NW region by measuring shot noise. Note that in reality only one lead is connected to the low temperature amplifier, so that switching between the reflection noise $S_{\rm R}$ and transmission noise $S_{\rm T}$ is achieved by interchanging the biased and floating N-terminals, see the SM for the wiring scheme. (c) Local differential conductance of NS junction in device NSN-II measured at $T=50\,{\rm mK}$ in different magnetic fields. (d) Non-local differential resistance $r_{21}\equiv dV_2/dI_1$ for two devices plotted at different B and $V_{\rm g}$.

gap $\Delta \approx 180 \, \mu \text{eV}$ of Al, the S terminal cannot absorb quasiparticles¹ and their non-equilibrium population can relax only via diffusion to the N terminals²⁶, manifesting charge-heat separation. This charge-neutral diffusion flux, which is referred to as the heat flux below, is shown by curly arrows in Fig. 1b. One part of the heat flux relaxes via terminal N1, similar to the usual two-terminal configurations^{27,28}. The other part bypasses the S terminal and relaxes via floating terminal N2. As we will demonstrate below, this transmitted heat flux can be detected by means of the shot noise thermometry.

For charge-heat separation via AR the quality of the InAs/Al interface is important, which we verify in transport measurements. In Fig. 1c we show the local differential conductance G_2 of the biased junction N2-S in device NSN-II as a function of voltage V_2 at a temperature $T=50\,\mathrm{mK}$. Without the magnetic field $(B)~G_2$ exhibits two well-defined maxima at finite V_2 that diminish

at increasing the B-field directed perpendicular to the substrate and vanish in $B\approx 20\,\mathrm{mT}$ simultaneously with the transition of the Al to the normal state. The maxima occur around gap edges $V_2=\pm\Delta/|e|$, where e is the elementary charge, and the corresponding increase of G_2 above the normal state value reaches about 15%. This re-entrant conductance behavior is a property of diffusive NS junctions with a highly transparent interface²⁹. Around zero bias in B=0 we generally observed a small reduction of G_2 by about 10% in all back gate voltage (V_g) range studied. This guarantees that possible residual reflectivity has a minor effect and ARs dominate over normal interface scattering in our devices.

In Fig. 1d we plot non-local differential resistance $r_{21} = dV_2/dI_1$, where V_2 is the voltage on terminal N2, as a function of V_1 . In the normal state r_{21} is featureless and consists of the interface resistance along with a few-Ohm contribution of the Al lead, see the trace in $B = 50 \,\mathrm{mT}$ in device NSN-I with $r_{21} \approx 40 \,\Omega$. By contrast, in B=0 strong gap-related features develop and r_{21} demonstrates local maximum and minima at the gap edges, see vertical arrows. Note that B = 0 behavior is non-universal and depending on $V_{\rm g}$ we have also observed bias asymmetry and sign reversal of the r_{21} , see two lower datasets for the device NSN-II. Most likely, these features have a thermoelectric origin as will be discussed below. Overall, r_{21} being small compared to the individual resistances of the NS junctions signals that the current transfer length $l_{\rm T}$ is small compared to the width of the S terminal. We estimate $l_{\rm T} \leq 100\,{\rm nm}$ close to the superconducting coherence length in Al, which sets the lowest possible bound for the $l_{\rm T}$, see SM for the details. r_{21} can be expressed via a non-diagonal element of the conductance matrix³⁰ as $r_{21} \approx -G_{12}/G_2G_1$, where $G_i \approx G_{ii} \ (i=1,2)$ are the two-terminal conductances of the NS junctions. $G_{12} \sim 10^{-2}G_i$ proves nearly perfect efficiency of the S contact as charge current sink.

Next, we probe the non-equilibrium electronic populations in both NS junctions using shot noise current fluctuations picked-up at different N-terminals in response to current in one of them. Fig. 2a demonstrates the noise spectral density measured in terminal N2 as a function of I_2 at two gate voltages. This configuration, referred to as the reflection configuration, is reminiscent of the usual AR noise in two-terminal devices^{27,28}, and the measured noise is denoted as $S_{\rm R}$. For comparison, a similar measurement in a reference NS device is shown in Fig. 2c. In both devices the results have much in common, the $S_{\rm R}$ scales linearly with current and exhibits clear kinks at the gap edges (marked by the arrows). Above the kinks, the diminished slope is the same and corresponds closely to the universal Fano factor in a diffusive conductor with normal leads $\delta S_{\rm R}/2e\delta I \approx 1/3$, as shown by the dashed lines with a marker "e". This familiar behavior¹² verifies elastic diffusive transport in InAs NWs³³ even at energies well above Δ and ensures quasiparticle relaxation by diffusion in contacts. However, at sub-gap biases we observe an important difference. While in the

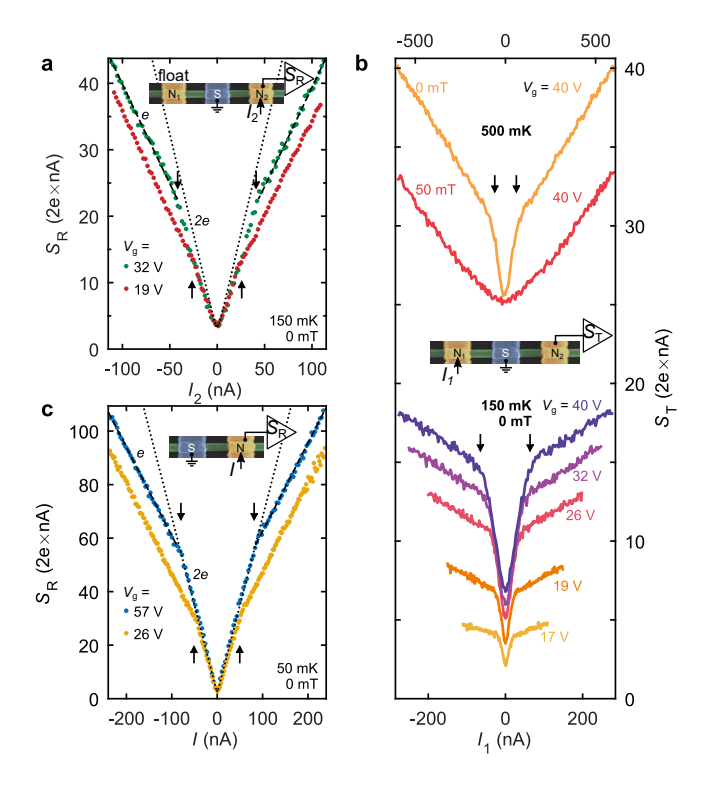


FIG. 2. Reflected and transmitted shot noise. (a) Reflection noise configuration in device NSN-I. Noise spectral density of the biased NS junction as a function of current at two values of $V_{\rm g}$. Dotted line is the fit with F=0.30 and charge q=2e; dashed line slope corresponds to F=0.30 and q=e. Green symbols are shifted vertically by $9\cdot 10^{-28}$ A²/Hz to coincide with red ones at zero bias. (b) Transmission noise configuration in device NSN-I. Noise spectral density of the floating NS junction as a function of current at different B,T and $V_{\rm g}$ (see legend). (c) Reflected shot noise in the reference two-terminal NS device as a function of current at two values of $V_{\rm g}$. Dotted line is the fit with F=0.33, q=2e; dashed line slope corresponds to F=0.33, q=e.

NS device the slope expectedly doubles 12,27 , see the dotted lines in Fig. 2c with a marker "2e", in the NSN device it increases much weaker such that $\delta S_{\rm R}/2e\delta I_2 \leq 0.5$, see Fig. 2a. Since doubled shot noise is a direct consequence of the reflection of heat flux at the S-terminal 26 , this means that the missing heat flux in the NSN device is transmitted towards the nearby floating NS junction. Similar behavior was previously observed in topological insulators 34 , however, in the present experiment the transmitted heat flux is directly measurable as we show below.

In Fig. 2b we plot the current dependencies of the shot noise measured in transmission configuration, $S_{\rm T}$, that is the noise at the floating terminal N2 in response to the current I_1 . Within all investigated $V_{\rm g}$ range, $S_{\rm T}$ steeply increases at small currents followed by pronounced kinks at the gap edges, see the arrows for some of the traces,

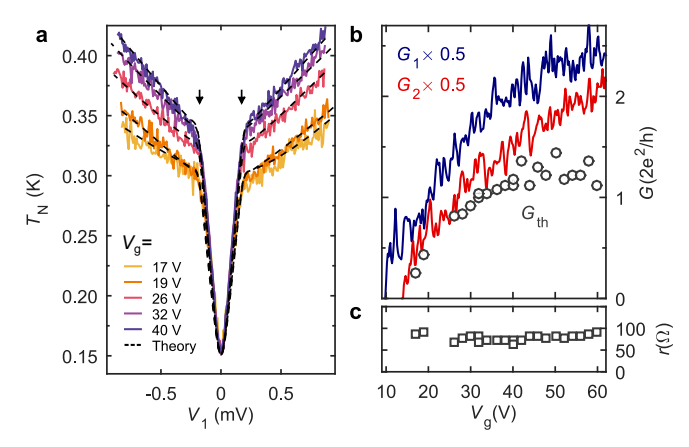


FIG. 3. Thermal conductance in the device NSN-I. (a) Noise temperature $T_{\rm N}$ measured in the transmission configuration as a function of bias (solid lines, same data as in the lower part of Fig. 2b) along with the model fits (dashed lines). (b) - (c) (symbols) Sub-gap thermal conductance $G_{\rm th}$ and interface resistance parameter r plotted as a function of $V_{\rm g}$. (lines) Linear response conductances of the left/right $G_{1/2}$ NS junctions.

and keeps increasing much weaker above the kinks. This behavior of $S_{\rm T}$ is explained as follows. Sub-gap quasiparticles diffusing along the superconductor, and experiencing a few ARs on the way, transmit the heat flux via proximitized InAs. Above-gap quasiparticles, however, mostly leave via the S terminal and their contribution to the transmitted heat signal is minimal. This qualitative picture is proved in the following crosscheck experiment. In the upper part of Fig. 2b, the $S_{\rm T}$ signals are compared in B=0 and $B=50\,\mathrm{mT}$ with the Al in superconducting and normal states, respectively. In the normal state S_T grows weakly at increasing I_1 without any kinks. Moreover above-gap signal in B=0 reproduces this trend up to a vertical shift at high I_1 . We conclude that above-gap heat transmission is not related to the superconductivity and is caused by residual normal interface scattering. Fig. 2b, therefore, demonstrates our main result that at sub-gap energies the proximitized In As NW supports transmission of heat underneath the S terminal by virtue of AR processes. Note also that for sub-gap energies $S_T \sim S_R$, cf. Fig. 2a, whereas non-local charge transport resulted in $|G_{12}| \ll G_1, G_2$. This difference emphasizes highly efficient charge-heat separation.

We proceed with a quantitative description of the Andreev heat transmission by solving the diffusion equation for the electronic energy distribution (EED), inspired by a quasiclassical approach²⁶. In the proximitized region the boundary conditions take into account ARs for the sub-gap transport and residual normal reflections above the gap. Thermal conductance $G_{\rm th}$ and interface resistance r are the only two parameters that, together with known G_1 , G_2 , determine the solution for the EED and the noise temperature $T_{\rm N}$ of the floating NS junction³⁵.

The details of theoretical modeling can be found in the Supplemental Material (SM). In Fig. 3a we compare the $T_{\rm N}$ measured in the experiment of Fig. 2b (solid lines) with the model fits (dashed lines). Plotted as a function of V_1 the kinks in $T_{\rm N}$ indeed occur at the gap edges for all $V_{\rm g}$ values, see the vertical arrows. The data is perfectly reproduced ensuring that our model captures correctly the physics of the Andreev heat transmission effect. The $V_{\rm g}$ dependence of the interface parameter r is shown in Fig. 3c. We find $r \sim 50 \Omega$, which is consistent with r_{21} in the same device in the normal state, cf. Fig. 1d, and almost independent of $V_{\rm g}$. The evolution of $G_{\rm th}$ at increasing $V_{\rm g}$ is shown by symbols in Fig. 3b. The initial growth is followed by saturation at $G_{\rm th} \sim e^2/h$. This is in contrast to a monotonic increase of the electrical conductances G_1, G_2 of NS junctions in the same device, see the lines in Fig. 3b. We attribute this difference to the impact of superconducting proximity effect that diminishes the density of states stronger at higher carrier densities.

So far we used shot noise measurements to demonstrate sub-gap Andreev heat transmission. In the following, we concentrate on the signatures of this effect in charge transport measurements in the device NSN-II. First, we focus on resistive thermometry based on a weak T-dependence of the mesoscopic conductance fluctuations. In Fig. 4a we plot the out-of-equilibrium linear response resistance $R_1 = \partial V_1/\partial I_1|_{I_1=0,I_2\neq 0}$ of the floating NS junction as a function of V_2 (see the upper sketch in Fig. 4 for the measurement configuration). R_1 exhibits the same qualitative behavior as the $S_{\rm T}$ before, with much stronger dependence at sub-gap energies, kinks at the gap edges and suppression in B-field. Using the equilibrium dependencies $R_1(T)$ for calibration, we converted this data in the effective temperature T^* of the floating NS junction and plotted in Fig. 4b. The behavior of T^* is similar to that of the T_N in the device NSN-I, cf. Fig. 3a, potentially making this approach an alternative for the detection of transmitted heat fluxes. Note, however, that resistive thermometry slightly underestimates the effect compared to a simultaneously measured T_N , see SM for the details of the analysis. This may be a result of dephasing that causes averaging of the conductance fluctuations and was not taken into account.

Finally, we investigate non-local I-V characteristics in the configuration shown in the lower sketch of Fig. 4. In Fig. 4c the voltage V_2 is plotted as a function of I_1 for three representative values of V_g . All traces lack full antisymmetry, $V_2(I_1) \neq -V_2(-I_1)$, moreover, the lower and upper traces exhibit local extrema near the origin, meaning that here the symmetric component dominates the I-V. This is a signature of the Andreev rectification effect³⁰, which also caused the asymmetry and sign reversal of r_{21} in Fig. 1d. Fig. 4d shows the symmetric component of the non-local voltage $V_2^{\text{symm}} \equiv [V_2(I_1) + V_2(-I_1)]/2$ against V_1 . V_2^{symm} evolves concurrently to the T^* and T_N with pronounced sub-gap behavior and kinks at $V_1 \approx \pm \Delta/e$, see vertical arrows. The

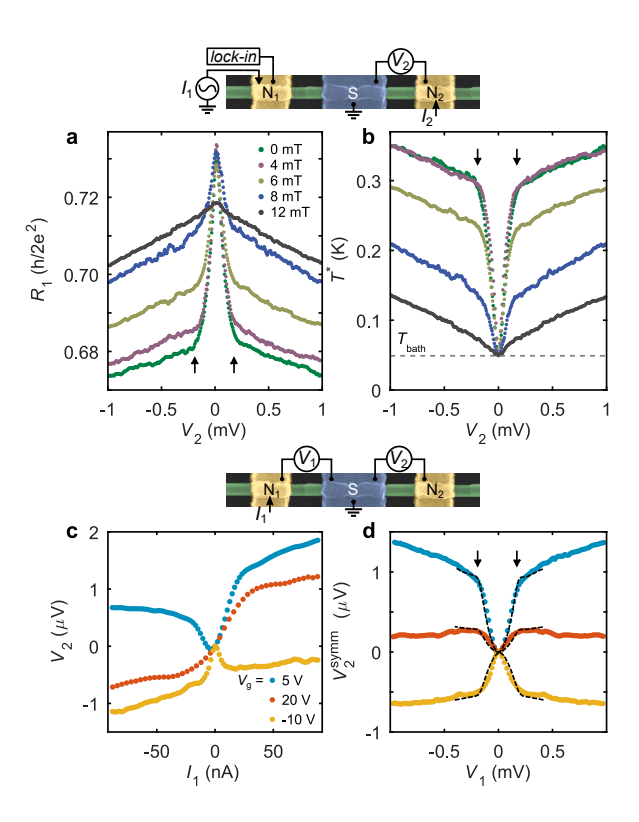


FIG. 4. Resistive thermometry and non-local I-Vs in device NSN-II. (a) Linear response resistance of the floating NS junction as a function of bias in the neighboring junction. (b) The same data converted to the effective temperature T^* . (c) The non-local I-V characteristics measured at three representative $V_{\rm g}$ values. (d) Symmetric component of the non-local I-Vs. The dashed lines are the calculated thermoelectric voltage values for different energy-independent Seebeck coefficients of $S/T=3.0\,\mu\text{V/K}^2$, $0.9\,\mu\text{V/K}^2$ and $-3.6\,\mu\text{V/K}^2$ (from top to bottom). Upper sketch: set up for resistive thermometry. Lower sketch: set up for non-local I-Vs.

signal is small, in $1\,\mu\mathrm{V}$ range, with both the sign and magnitude demonstrating strong V_{g} -dependent fluctuations, in contrast to T^* and T_{N} . We suggest that the finite V_2^{symm} has a thermoelectric origin and results from the thermal gradient that builds up in response to the transmitted heat flux. Indeed, the data of Fig. 4d is consistent with V_{g} fluctuations of the Seebeck coefficient 36,37 in the range $|S/T|\sim 5\,\mu\mathrm{V/K^2}$, corresponding fits shown by the dashed lines (see SM for the details). Note that the degree of asymmetry of the non-local conductance $G_{12} \propto -(dV_2/dI_1)$ caused by this effect (see Fig. 1d) is comparable to the data in a Cooper pair splitter 38 and in a tunnel-coupled Majorana device 39 . Our thermoelectric interpretation may also turn useful in explaining these data.

The DC transport data of Fig. 4 reveals the effect of the heat-mode excitation in a proximity superconductor only indirectly, via a weak and non-universal energydependence of the spectral conductance. This is in stark contrast to our shot noise approach, that senses the randomness caused by the non-equilibrium EED itself, without the need for any type of spectral resolution⁴⁰. In the same way, the shot noise can also probe excitations of different origin, e.g. spin currents in superconducting spintronics⁴¹, or even valley currents⁴², by virtue of spontaneous fluctuations that arise when such currents are fed into the adjacent normal lead^{43–45}. From this perspective, our experiment establishes a natural background to probe charge-neutral excitations, both above-gap in bulk

superconductors and sub-gap in proximity superconductors, including the proposed detection of Majorana zero modes in heat transport $^{46-50}$.

We are grateful to S.M. Frolov, T.M. Klapwijk, S. Ludwig, A.S. Mel'nikov and K.E. Nagaev for helpful discussions. This work was financially supported by the RSF project 19-12-00326 (fabrication of the NSN devices, transport characterization and shot noise measurements) and RFBR project 19-02-00898 (fabrication of the NS device, non-local charge-transport measurements). Theoretical modeling was performed under the state task of the ISSP RAS.

- ¹ A. F. Andreev, JETP Letters **46**, 1823 (1964).
- ² C. Caroli, P. D. Gennes, and J. Matricon, Physics Letters 9, 307 (1964).
- ³ M. Titov, A. Ossipov, and C. W. J. Beenakker, Phys. Rev. B **75**, 045417 (2007).
- ⁴ G.-H. Lee, K.-F. Huang, D. K. Efetov, D. S. Wei, S. Hart, T. Taniguchi, K. Watanabe, A. Yacoby, and P. Kim, Nature Physics 13, 693 (2017).
- ⁵ L. Zhao, E. G. Arnault, A. Bondarev, A. Seredinski, T. F. Q. Larson, A. W. Draelos, H. Li, K. Watanabe, T. Taniguchi, F. Amet, H. U. Baranger, and G. Finkelstein, Nature Physics (2020), 10.1038/s41567-020-0898-5.
- ⁶ M. Banerjee, M. Heiblum, A. Rosenblatt, Y. Oreg, D. E. Feldman, A. Stern, and V. Umansky, Nature **545**, 75 (2017).
- ⁷ C. W. J. Beenakker, Phys. Rev. Lett. **97**, 067007 (2006).
- ⁸ N. B. Kopnin, A. S. Mel'nikov, and V. M. Vinokur, Phys. Rev. B **70**, 075310 (2004).
- ⁹ M. Tinkham, Introduction to Superconductivity, Dover Books on Physics Series (Dover Publications, 2004).
- ¹⁰ L. Hofstetter, S. Csonka, J. Nygård, and C. Schnenberger, Nature 461, 960 (2009).
- ¹¹ L. G. Herrmann, F. Portier, P. Roche, A. L. Yeyati, T. Kontos, and C. Strunk, Phys. Rev. Lett. **104**, 026801 (2010).
- A. Das, Y. Ronen, M. Heiblum, D. Mahalu, A. V. Kretinin, and H. Shtrikman, Nature Communications 3, 1165 EP (2012), article.
- ¹³ R. M. Lutchyn, J. D. Sau, and S. Das Sarma, Phys. Rev. Lett. **105**, 077001 (2010).
- Y. Oreg, G. Refael, and F. von Oppen, Phys. Rev. Lett. 105, 177002 (2010).
- ¹⁵ S. M. Albrecht, A. P. Higginbotham, M. Madsen, F. Kuemmeth, T. S. Jespersen, J. Nygård, P. Krogstrup, and C. M. Marcus, Nature **531**, 206 (2016).
- ¹⁶ M. T. Deng, S. Vaitiekenas, E. B. Hansen, J. Danon, M. Leijnse, K. Flensberg, J. Nygård, P. Krogstrup, and C. M. Marcus, Science 354, 1557 (2016).
- P. Yu, J. Chen, M. Gomanko, G. Badawy, E. P. A. M. Bakkers, K. Zuo, V. Mourik, and S. M. Frolov, "Non-majorana states yield nearly quantized conductance in superconductor-semiconductor nanowire devices," (2020), arXiv:2004.08583 [cond-mat.mes-hall].
- ¹⁸ S. Vaitiekėnas, G. W. Winkler, B. van Heck, T. Karzig, M.-T. Deng, K. Flensberg, L. I. Glazman, C. Nayak, P. Krogstrup, R. M. Lutchyn, and C. M. Marcus, Science

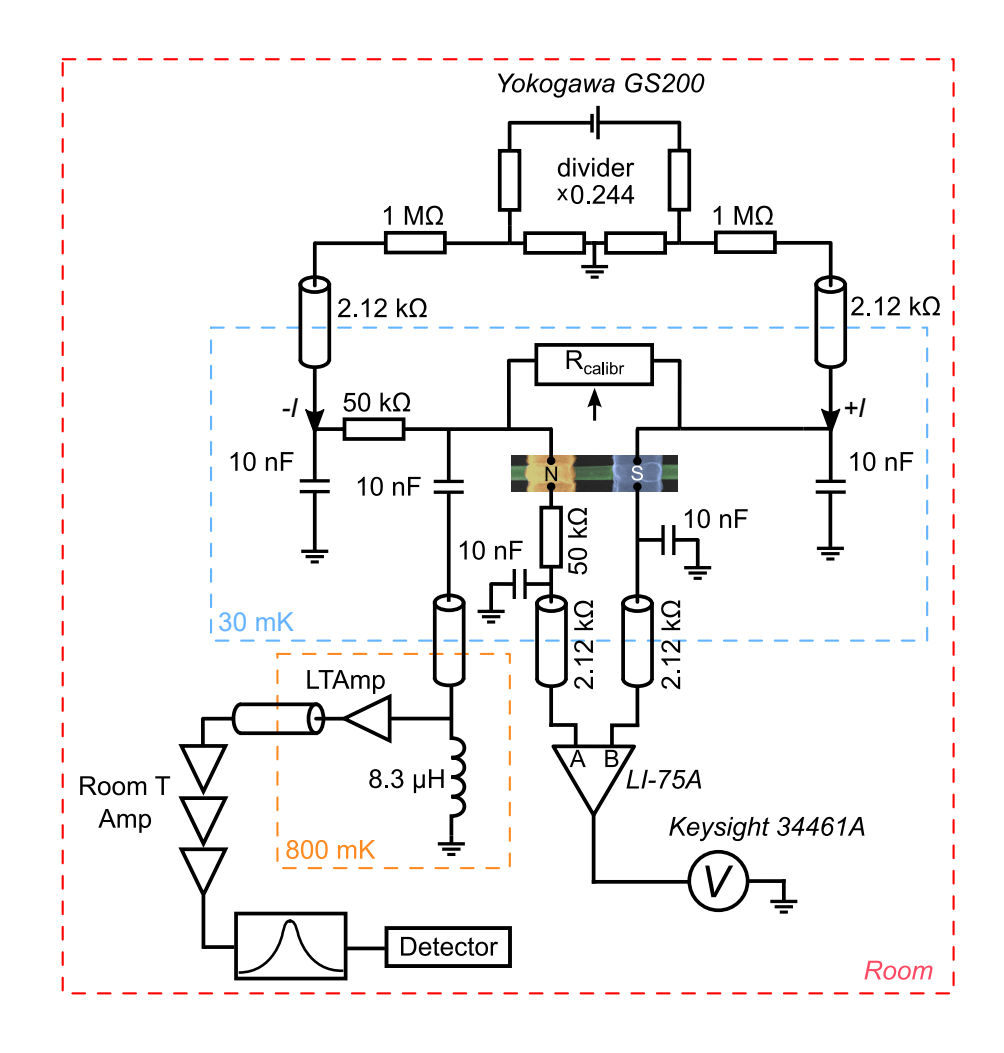
- **367**, eaav3392 (2020).
- ¹⁹ A. A. Kopasov and A. S. Mel'nikov, Phys. Rev. B **101**, 054515 (2020).
- ²⁰ R. S. Keizer, M. G. Flokstra, J. Aarts, and T. M. Klapwijk, Phys. Rev. Lett. **96**, 147002 (2006).
- ²¹ F. Hübler, J. C. Lemyre, D. Beckmann, and H. v. Löhneysen, Phys. Rev. B 81, 184524 (2010).
- N. Vercruyssen, T. G. A. Verhagen, M. G. Flokstra, J. P. Pekola, and T. M. Klapwijk, Phys. Rev. B 85, 224503 (2012).
- T. E. Golikova, M. J. Wolf, D. Beckmann, I. E. Batov, I. V. Bobkova, A. M. Bobkov, and V. V. Ryazanov, Phys. Rev. B 89, 104507 (2014).
- ²⁴ F. S. Bergeret, M. Silaev, P. Virtanen, and T. T. Heikkilä, Rev. Mod. Phys. **90**, 041001 (2018).
- M. Kuzmanovi, B. Y. Wu, M. Weideneder, C. H. L. Quay, and M. Aprili, "Evidence for spin-dependent energy transport in a superconductor," (2020), arXiv:2001.04422 [cond-mat.mes-hall].
- ²⁶ K. E. Nagaev and M. Büttiker, Phys. Rev. B **63**, 081301 (2001).
- A. A. Kozhevnikov, R. J. Schoelkopf, and D. E. Prober, Phys. Rev. Lett. 84, 3398 (2000).
- ²⁸ X. Jehl, M. Sanquer, R. Calemczuk, and D. Mailly, Nature 405, 50 (2000).
- ²⁹ H. Courtois, P. Charlat, P. Gandit, D. Mailly, and B. Pannetier, Journal of Low Temperature Physics **116**, 187 (1999).
- ³⁰ T. O. Rosdahl, A. Vuik, M. Kjaergaard, and A. R Akhmerov, Phys. Rev. B **97**, 045421 (2018).
- ³¹ A. H. Steinbach, J. M. Martinis, and M. H. Devoret, Phys. Rev. Lett. **76**, 3806 (1996).
- ³² M. Henny, S. Oberholzer, C. Strunk, and C. Schönenberger, Phys. Rev. B 59, 2871 (1999).
- ³³ E. S. Tikhonov, D. V. Shovkun, D. Ercolani, F. Rossella, M. Rocci, L. Sorba, S. Roddaro, and V. S. Khrapai, Scientific Reports 6, 30621 EP (2016), article.
- ³⁴ E. S. Tikhonov, D. V. Shovkun, M. Snelder, M. P. Stehno, Y. Huang, M. S. Golden, A. A. Golubov, A. Brinkman, and V. S. Khrapai, Phys. Rev. Lett. 117, 147001 (2016).
- ³⁵ K. Nagaev, Physics Letters A **169**, 103 (1992).
- ³⁶ P. M. Wu, J. Gooth, X. Zianni, S. F. Svensson, J. G. Gluschke, K. A. Dick, C. Thelander, K. Nielsch, and H. Linke, Nano Letters 13, 4080 (2013).
- ³⁷ E. S. Tikhonov, D. V. Shovkun, D. Ercolani, F. Rossella, M. Rocci, L. Sorba, S. Roddaro, and V. S. Khrapai, Semi-

- conductor Science and Technology 31, 104001 (2016).
- ³⁸ L. Hofstetter, S. Csonka, A. Baumgartner, G. Fülöp, S. d'Hollosy, J. Nygård, and C. Schönenberger, Phys. Rev. Lett. **107**, 136801 (2011).
- ³⁹ G. C. Ménard, G. L. R. Anselmetti, E. A. Martinez, D. Puglia, F. K. Malinowski, J. S. Lee, S. Choi, M. Pendharkar, C. J. Palmstrøm, K. Flensberg, C. M. Marcus, L. Casparis, and A. P. Higginbotham, Phys. Rev. Lett. 124, 036802 (2020).
- ⁴⁰ E. S. Tikhonov, A. O. Denisov, S. U. Piatrusha, I. N. Khrapach, J. P. Pekola, B. Karimi, R. N. Jabdaraghi, and V. S. Khrapai, "Energy resolution of electronic states delivered by pauli exclusion and shot noise," (2020), arXiv:2001.07563 [cond-mat.mes-hall].
- ⁴¹ J. Linder and J. W. A. Robinson, Nature Physics **11**, 307 (2015).
- ⁴² J. R. Schaibley, H. Yu, G. Clark, P. Rivera, J. S. Ross, K. L. Seyler, W. Yao, and X. Xu, Nature Reviews Materials 1 (2016), 10.1038/natrevmats.2016.55.

- ⁴³ J. Meair, P. Stano, and P. Jacquod, Phys. Rev. B **84**, 073302 (2011).
- ⁴⁴ V. S. Khrapai and K. E. Nagaev, JETP Letters **105**, 18 (2017).
- ⁴⁵ T. Ludwig, I. S. Burmistrov, Y. Gefen, and A. Shnirman, Phys. Rev. Research 2, 023221 (2020).
- ⁴⁶ N. Read and D. Green, Phys. Rev. B **61**, 10267 (2000).
- ⁴⁷ Z. Wang, X.-L. Qi, and S.-C. Zhang, Phys. Rev. B **84**, 014527 (2011).
- ⁴⁸ A. R. Akhmerov, J. P. Dahlhaus, F. Hassler, M. Wimmer, and C. W. J. Beenakker, Phys. Rev. Lett. **106**, 057001 (2011).
- ⁴⁹ D. Bagrets, A. Altland, and A. Kamenev, Phys. Rev. Lett. 117, 196801 (2016).
- Y. Kasahara, T. Ohnishi, Y. Mizukami, O. Tanaka, S. Ma, K. Sugii, N. Kurita, H. Tanaka, J. Nasu, Y. Motome, T. Shibauchi, and Y. Matsuda, Nature 559, 227 (2018).

Supplemental Material

Noise and charge transport measurements

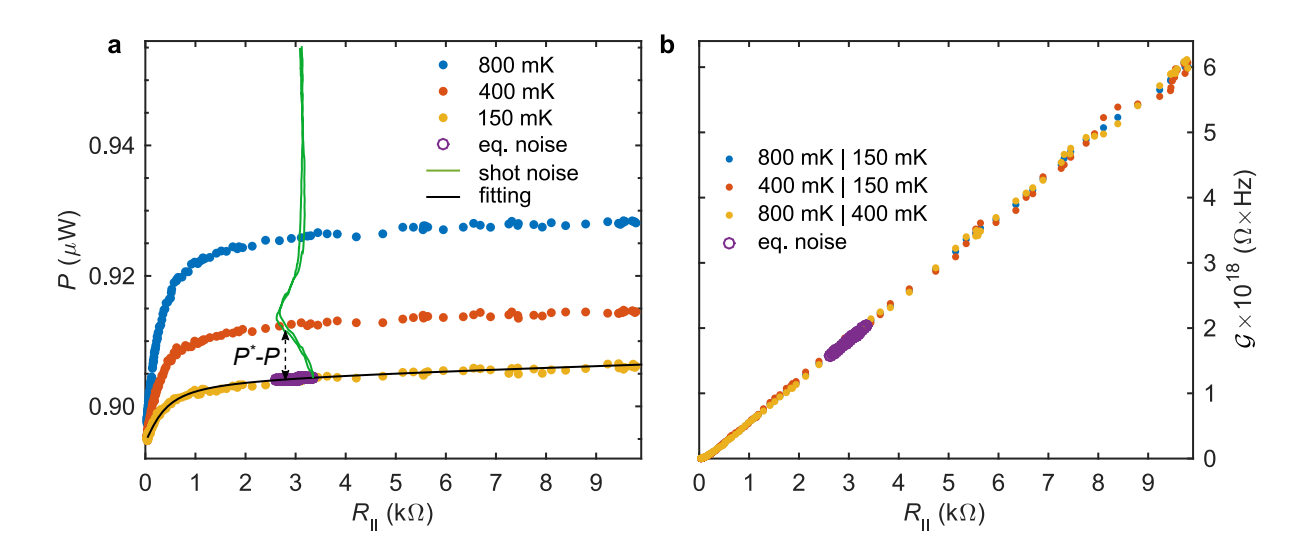


Supplemental Material Fig. 1. Sketch of the noise setup.

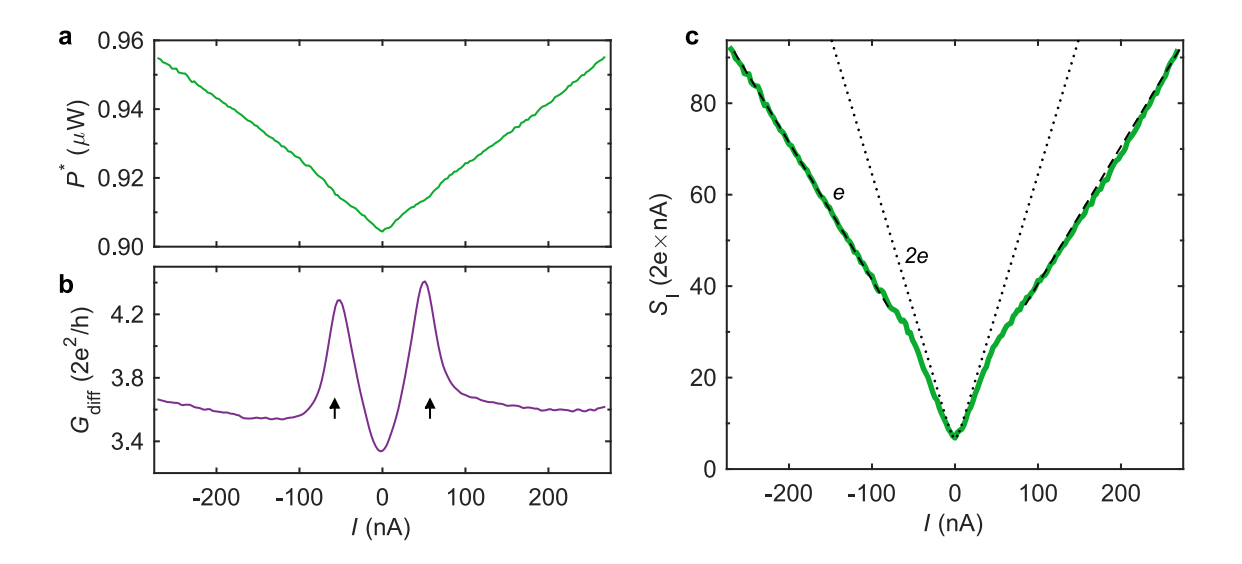
DC and low frequency AC transport measurements are carried out using symmetric current bias scheme with divider shown in Fig. 1. We use quasi-4-terminal setup thus excluding wiring and filtering contribution into measured voltage signal. We use SR-7265 lock-in for resistive thermometry with typical modulation current of 2 nA, f = 19.3 Hz, time constant = 2s, AC gain 30 dB and filter slope of 24 dB/oct.

The noise spectral density was measured using the home-made low-temperature amplifier (LTamp) with a voltage gain of about 10 dB and the input current noise of $\sim 2\text{--}6\times 10^{-27}~\text{A}^2/\text{Hz}$. The voltage fluctuations on a 25 k Ω load resistance were measured near the central frequency 14.2 MHz (± 0.6 MHz for -3 dB point) of a resonant circuit at the input of the LTAmp. The output of the LTamp was fed into the low noise 75 dB gain room temperature amplification stage followed by a hand-made analogue band-pass filter and a power detector. The setup was calibrated using HEMT ATF-35143 as adjustable load $R_{\rm calib} = 50~\Omega \rightarrow > 100~\text{M}\Omega$ for the equilibrium Johnson-Nyquist noise thermometry. Except for the periods of calibration, the transistor was always kept pinched off. Unless otherwise stated, the measurements were performed in a cryogenic free Bluefors dilution refrigerator BF-LD250 at a bath temperature of 30 mK.

Johnson-Nyquist noise thermometry



Supplemental Material Fig. 2. Calibration via equilibrium noise. (a) Power released on the detector as a function of total load resistance $R_{||}$ measured at different bath temperatures (see electron temperature in the legend). Green solid line shows typical reflected shot-noise signal at applying bias current through the device (NSN - I, $V_g = 40$ V). Black solid line is fit using Nyquist relation. Purple circles shows bias-dependent gain and equilibrium noise. (b) Total gain of the setup. Three sets of points correspond to three different combinations of $T_1|T_2$ (see text below).



Supplemental Material Fig. 3. **Shot-noise.** (a) Power dissipated in the detector is plotted as a function of current through the sample. (b) Differential conductance of the NS junction. Arrows mark superconducting gap $\pm \Delta$. (c) Extracted current noise spectral density. Dashed line corresponds to Fano-factor $F = S_{\rm I}/2eI = 0.30$ and $e^* = e$, dotted line is for doubled charge -F = 0.30 and -F = 0.30 a

We calibrate our setup using equilibrium noise thermometry. At zero current through the device, we are able to change a value of $R_{||} = (G_{\text{diff}} + R_{\text{25k}\Omega}^{-1} + R_{\text{calibr}}^{-1})^{-1}$ drastically, where G_{diff} is a differential resistance (zero bias) of the sample shown in Fig. 3b. Power released on the detector after all amplification stages :

$$P(R_{||}) = \left(\frac{4k_{\rm B}T}{R_{||}} + S_{\rm I}^{\rm Amp}\right) \int \frac{G \times Tr^{\rm filter}(f)}{R_{||}^{-2} + |Z_{\rm LC}|^{-2}} df + P_0 = \mathcal{G}(R_{||}) \left(\frac{4k_{\rm B}T}{R_{||}} + S_{\rm I}^{\rm Amp}\right) + P_0$$
 (S1)

where G is an unknown total gain, Z_{LC} - complex impedance of the LC contour, $Tr^{\text{filter}}(f)$ - transmission characteristic of the band-pass filter, $S_{\text{I}}^{\text{Amp}}$ and P_0 - parasitic current noise and background of the low-temperature amplifier. After an integration over frequency, we can use generalized value for gain $\mathcal{G}(R_{||})$ which can be extracted by measuring $P(R_{||})$ at different bath temperatures:

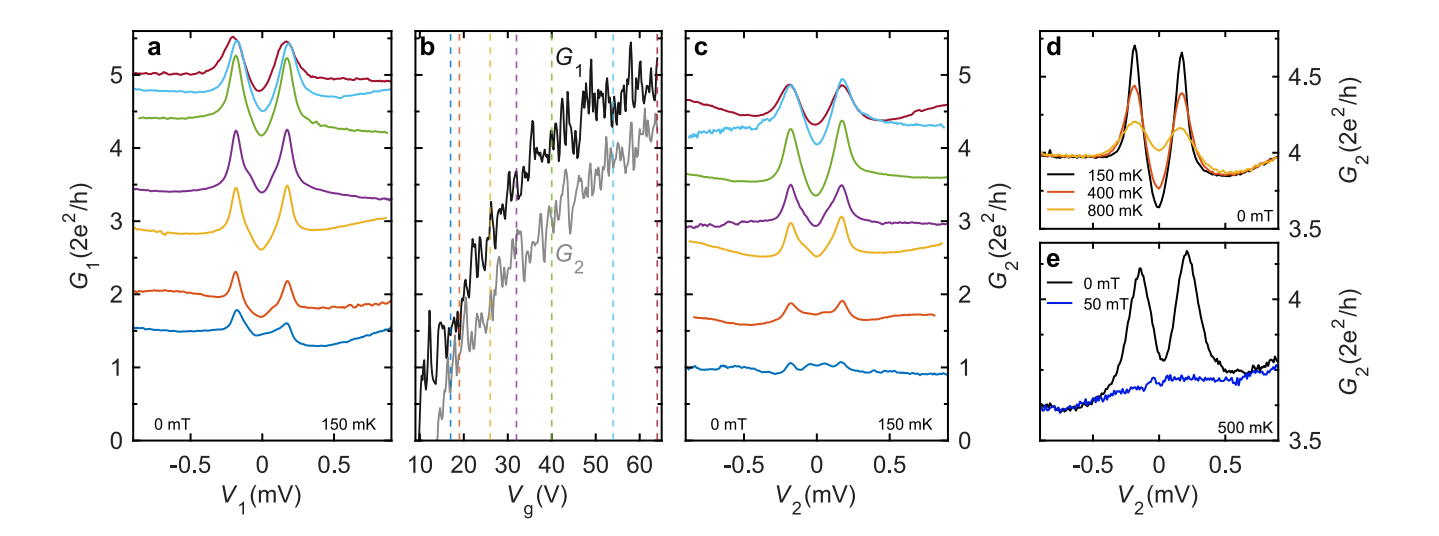
$$\mathcal{G}(R_{||}) = \frac{P(R_{||}, T_1) - P(R_{||}, T_2)}{T_1 - T_2} \frac{R_{||}}{4k_B}$$
(S2)

When we apply current through the sample, the crossover from thermal to non-equilibrium shot noise (see solid green curve in Fig. 2a and Fig. 3a) appears. Depending on the bias current, $R_{||}(I)$ is changing thus making $\mathcal{G}(R_{||})$ bias-dependent (see purple symbols in Fig. 2a, b). Desired current noise of the sample $S_{\rm I}$ contributes to the total power as follows (transistor is pinched off $R_{\rm calib} > 100~{\rm M}\Omega$):

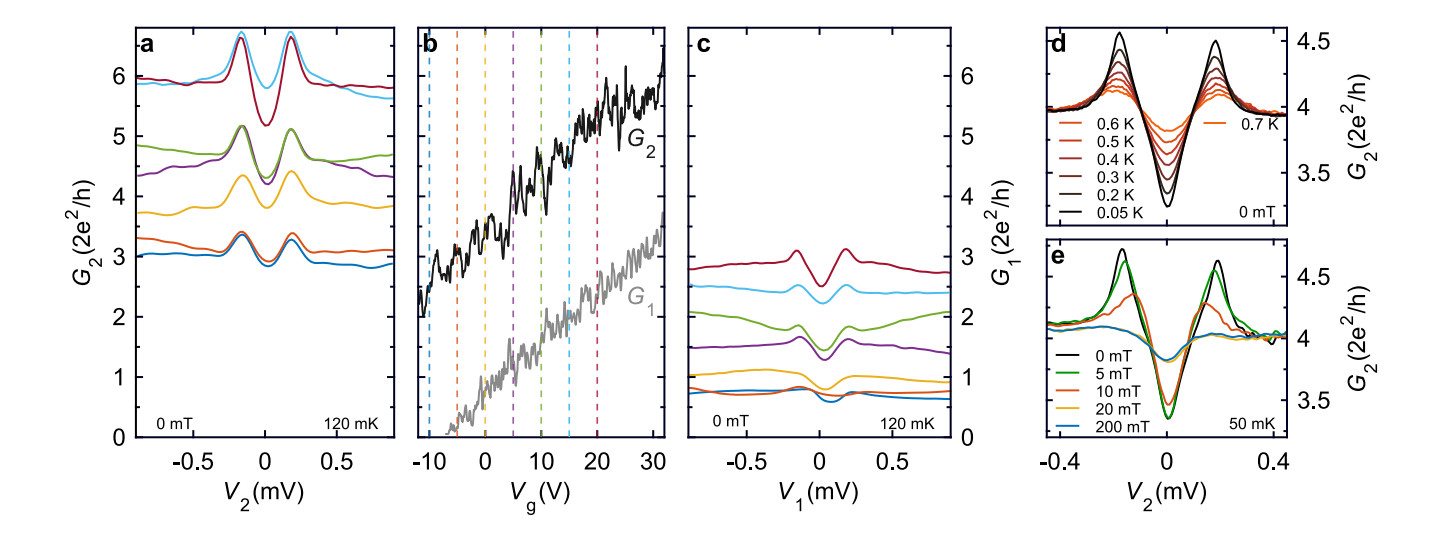
$$P^*(R_{||}) = \mathcal{G}(R_{||}) \left(\frac{4k_{\rm B}T}{R_{25k\Omega}} + S_{\rm I} + S_{\rm I}^{\rm Amp} \right) + P_0, \quad S_{\rm I} = \frac{P^*(R_{||}) - P(R_{||})}{\mathcal{G}(R_{||})} + 4k_{\rm B}TG_{\rm diff}$$
 (S3)

Finalized current spectral density curve is shown in Fig. 3c.

Local charge transport

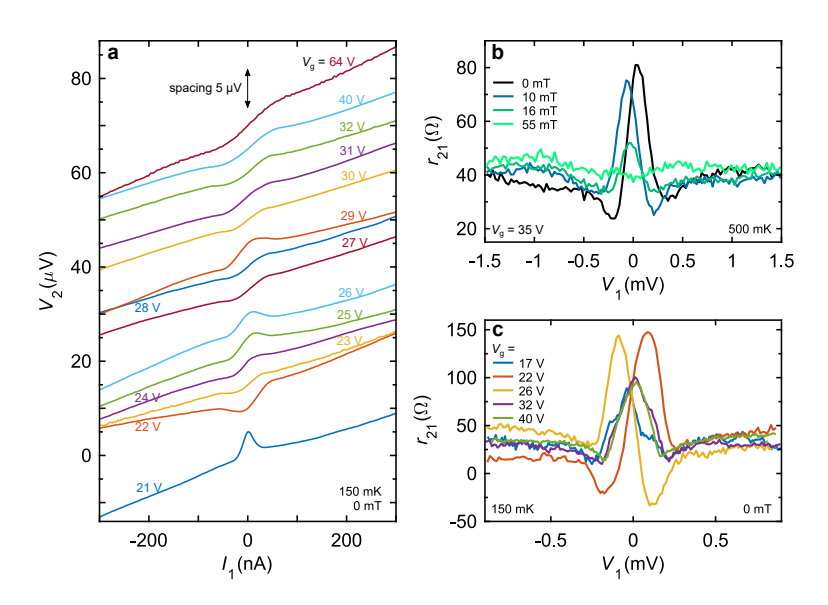


Supplemental Material Fig. 4. NSN - I. (a) and (c) Local spectral conductance of the left and right NS junctions correspondingly, measured at different back-gate voltages $V_{\rm g}=17,\ 19$, 26, 32, 40, 54, 64 V from bottom to top. (b) Linear-response conductance is plotted as function of $V_{\rm g}$. Dashed lines of corresponding colors point certain values of back-gate voltages from (a) and (c). (d) and (e) Temperature and magnetic field dependence of the spectral conductance measured at constant $V_{\rm g}=41$ and 50 V correspondingly.

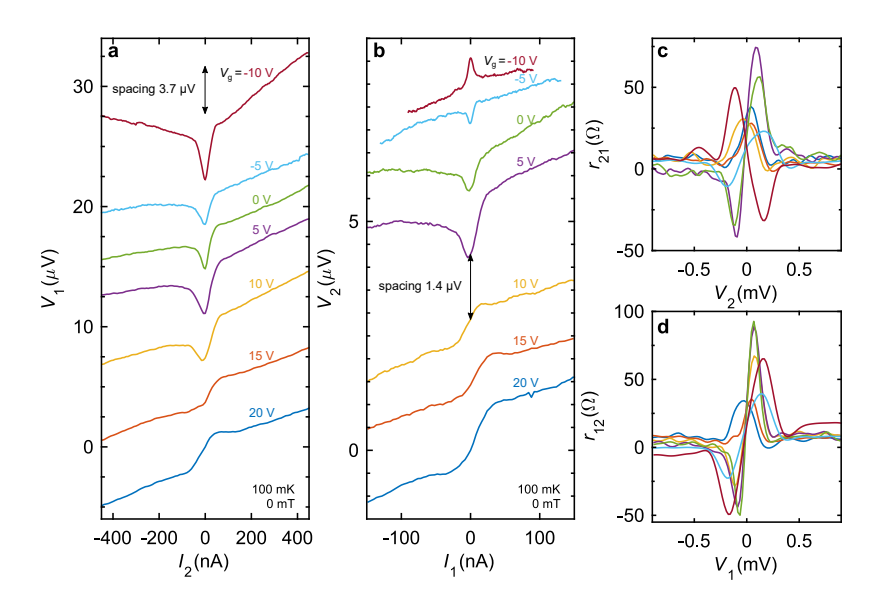


Supplemental Material Fig. 5. NSN - II. (a) and (c) Local spectral conductance of the left and right NS junctions correspondingly, measured at different back-gate voltages $V_{\rm g}=-10, -5, 0, 5, 10, 15, 20$ V from bottom to top. (b) Linear-response conductance is plotted as function of $V_{\rm g}$. Dashed lines of corresponding colors point certain values of back-gate voltages from (a) and (c). (d) and (e) Temperature and magnetic field dependence of the spectral conductance measured at constant $V_{\rm g}=0$ V.

Non-local charge transport

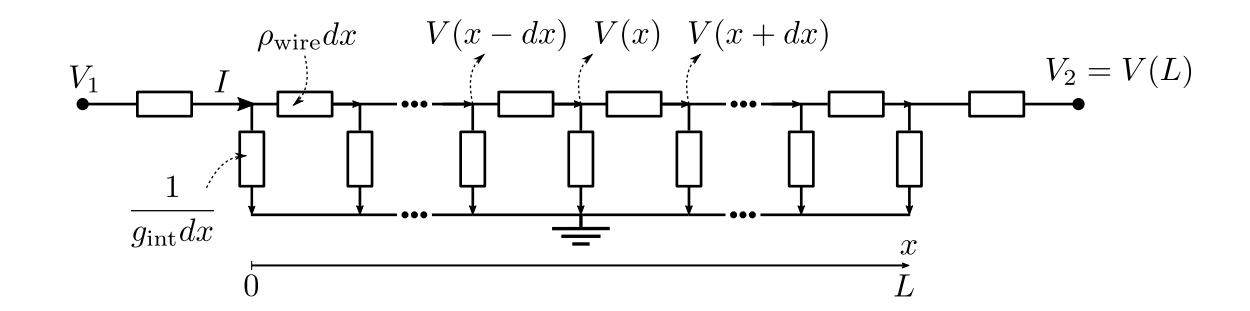


Supplemental Material Fig. 6. **NSN - I.** (a) Non-local I/V characteristics measured at different back-gate voltages. For convenience, curves are shifted vertically with spacing of 5 μ V. (b) and (c) Differential non-local resistance $r_{21} = dV_2/dI_1$, $I_2 = 0$ at different magnetic fields and back-gate voltages correspondingly.



Supplemental Material Fig. 7. **NSN - II.** (a) and (b) Non-local I/V characteristics of both NS junctions measured at different back-gate voltages. For convenience, curves are shifted vertically with spacing of 3.7 μ V and 1.4 μ V correspondingly. (c) and (d) Differential non-local resistance $r_{21} = dV_2/dI_1$, $I_2 = 0$ and $r_{12} = dV_1/dI_2$, $I_1 = 0$ at different back-gate voltages. Colors match those from (a) and (b).

Current transfer length estimation



Supplemental Material Fig. 8. Effective resistance model for nanowire/superconductor interface.

To estimate the characteristic length of charge overflow within grounded S terminal $l_{\rm T}$ we use circuit shown in fig. 8. Here $\rho_{\rm wire}$ and $g_{\rm int}$ are resistance of the nanowire (NW) and conductivity of interface per unit length respectively. In the continuous limit we can write current conservation for each point along NW/S interface:

$$\frac{V(x+dx) - V(x)}{\rho_{\text{wire}} dx} + \frac{V(x-dx) - V(x)}{\rho_{\text{wire}} dx} = \frac{V(x)dx}{1/g_{\text{int}}}$$
$$\frac{d^2 V(x)}{dx^2} = \frac{V(x)}{l_{\text{T}}^2}, \quad l_{\text{T}} = \frac{1}{\sqrt{\rho_{\text{wire}} g_{\text{int}}}}$$

Boundary conditions including one that normal terminal N2 is floating and no current flow into it.

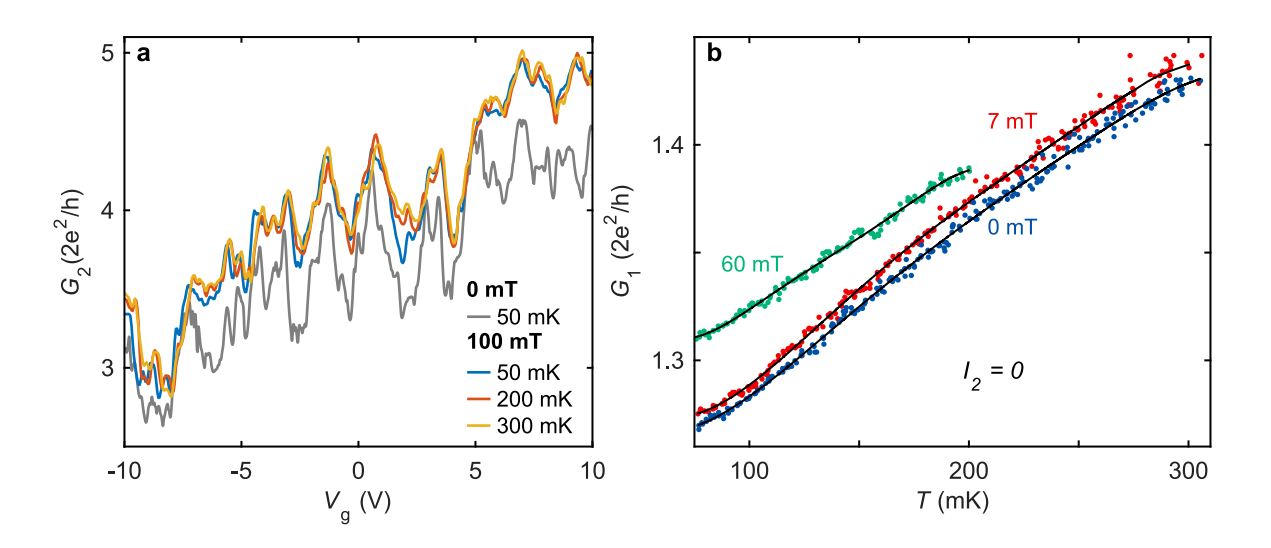
$$\left.\frac{dV(x)}{dx}\right|_{x=0} = -\rho_{\rm wire}I, \ \left.\frac{dV(x)}{dx}\right|_{x=L} = 0$$

Solving elementary Neumann problem we can find non-local ristance r_{21} :

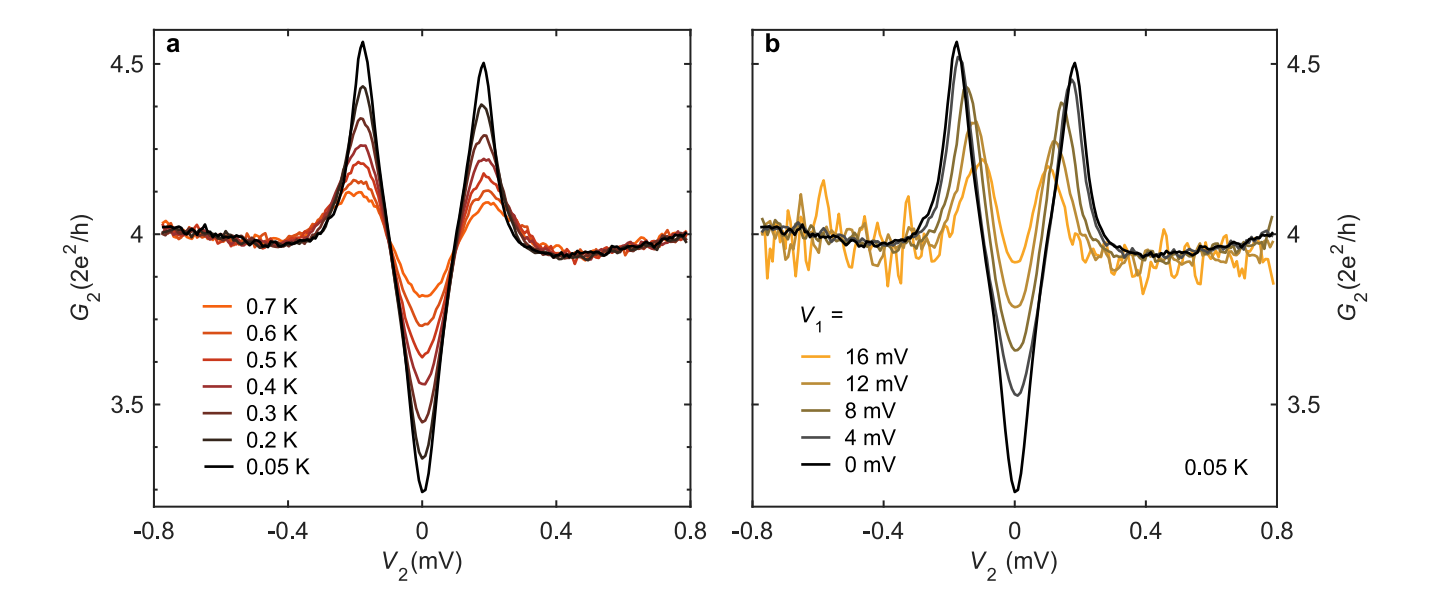
$$r_{21} = \frac{V(L)}{I} = \frac{l_{\rm T}\rho_{\rm wire}}{\sinh(\frac{L}{l_{\rm T}})}$$

For two measured devices (NSN-I, NSN-II) we have $r_{21} \approx 40$, 10Ω and $L \approx 200$, $300 \, \mathrm{nm}$ respectively, thus $l_{\mathrm{T}} \approx 75 \, \mathrm{nm}$.

Temperature dependence of differential conductance.

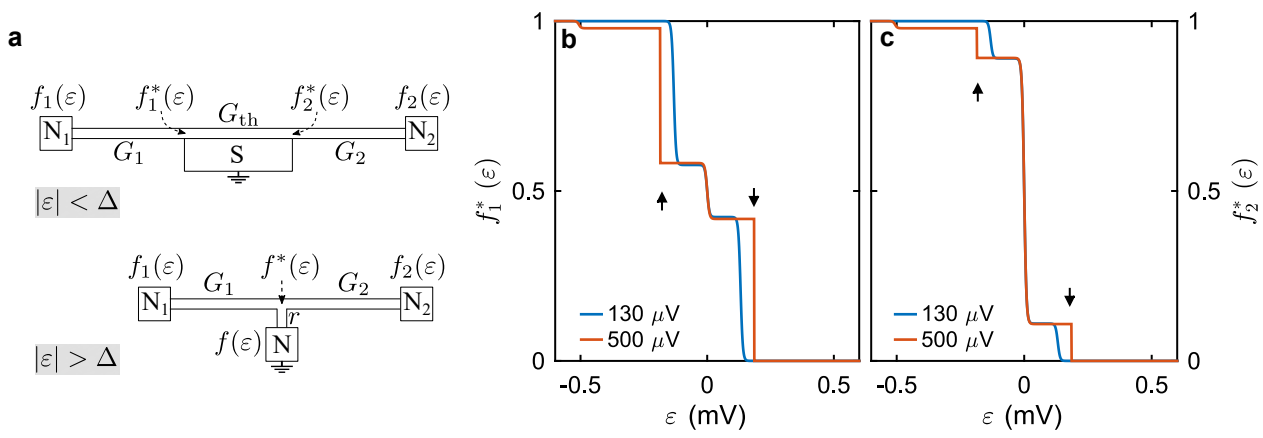


Supplemental Material Fig. 9. Linear regime and calibration. (a) Linear-response conductance of a single NS junction (NSN - II device) measured at different bath temperatures. Overall increasing dependence with reproducible UCF persists up to the shift $\sim 10\%$ when large magnetic field ($100\,\mathrm{mT} > B_\mathrm{c}$) is applied. Such zero-bias deep is more evident from differential conductance data measured at $V_\mathrm{g} = 0\,\mathrm{V}$ and $I_2 = 0$ shown in (b). Solid lines are smooth polynomial fits we use for the resistive thermometry.



Supplemental Material Fig. 10. Non-linear regime. (a) Spectral conductance measured at constant $V_{\rm g}=0$ V (NSN - II device) and different bath temperatures. (b) Spectral conductance measured at constant $V_{\rm g}=0$ V, bath temperature but different "heating" voltages across the adjacent NS junction.

Analytical model



Supplemental Material Fig. 11. (a) Schematics of the analytical model, separately for sub-gap and above-gap quasiparticle energies. (b) - (c) Calculated EEDs near two ends of the proximitized sections for $V_1 = 130~\mu V$ and 500 μV (T = 50~mK, $G_{\text{th}} = 1.17 \times 2e^2/h$, $r = 64~\Omega$). Arrows mark the superconducting gap of Al, $\Delta = 180~\mu V$.

The sketch of analytical model we use to fit experimental data is shown in fig.3a. Since we operate in the non-linear $\varepsilon_T \sim k_{\rm B}T \ll eV$ regime, where $\xi_T = \hbar D/L^2 \approx 15\,\mu{\rm V}$ is the Thouless energy, we can neglect the penetration of the condensate into NW and consider it just as a normal metal with a non-equilibrium electronic energy distribution (EED). Distribution functions near the N terminals $f_{1/2}(\varepsilon)$ are equilibrium Fermi-Dirac functions with local temperature and chemical potential of the corresponding terminal. EED near S should satisfy Andreev conditions for the energies below the gap:

$$f_{1/2}^*(\varepsilon) = \begin{cases} 1 - f_{1/2}^*(-\varepsilon) & |\varepsilon| < \Delta \\ (\exp(\varepsilon/k_{\rm B}T) + 1)^{-1} & |\varepsilon| > \Delta \end{cases}$$
 (S4)

Following Nagaev and Buttiker [S1] we separately find electron distribution functions for energies below and above the gap and then sew them together:

$$f(\varepsilon) = f^{\text{ingap}}(\varepsilon)\theta(\Delta - |\varepsilon|) + f^{\text{outgap}}(\varepsilon)\theta(|\varepsilon| - \Delta)$$
(S5)

Sub-gap (
$$|\varepsilon| < \Delta$$
)

First we calculate for energies within the superconducting gap. Since noise temperature gradient is zero at N/S interface, then the correction to the noise temperature due to the finite r is of the second order and we can neglect it. In order to find the energy distributions $f_1^*(\varepsilon)$ and $f_1^*(\varepsilon)$ at the two ends of the proximitized wire section, one has to fulfill the continuity of the heat fluxes in these points at any given ε . In this way we get the following two equations:

$$G_2[f_2(\varepsilon) - f_2^*(\varepsilon)] - G_2[f_2(-\varepsilon) - f_2^*(-\varepsilon)] = G_{\text{th}}[f_2(\varepsilon) - f_1^*(\varepsilon)] - G_{\text{th}}[f_2(-\varepsilon) - f_1^*(-\varepsilon)]$$
(S6)

$$G_1[f_1(\varepsilon) - f_1^*(\varepsilon)] - G_1[f_1(-\varepsilon) - f_1^*(-\varepsilon)] = G_{th}[f_2(\varepsilon) - f_1^*(\varepsilon)] - G_{th}[f_2(-\varepsilon) - f_1^*(-\varepsilon)]$$
(S7)

where the terms with ε correspond to the particle heat flux and the terms with $-\varepsilon$ to the hole heat flux. The equations (S6) and (S7) are for the right and the left NS interface respectively. For convinience lets introduce $F(\varepsilon) \equiv f(\varepsilon) - f(-\varepsilon)$, then:

$$F_{1}^{*}(\varepsilon) = \frac{G_{1}G_{2}F_{1}(\varepsilon) + G_{\text{th}}G_{2}F_{1}(\varepsilon) + G_{\text{th}}G_{2}F_{2}(\varepsilon)}{G_{\text{th}}G_{1} + G_{\text{th}}G_{2} + G_{1}G_{2}}, \quad F_{2}^{*}(\varepsilon) = \frac{G_{1}G_{2}F_{2}(\varepsilon) + G_{\text{th}}G_{2}F_{2}(\varepsilon) + G_{\text{th}}G_{1}F_{1}(\varepsilon)}{G_{\text{th}}G_{1} + G_{\text{th}}G_{2} + G_{1}G_{2}}$$
(S8)

Since $f_i^*(\varepsilon) = 1 - f_i^*(-\varepsilon)$, we can easily find $f_i^* = (1 + F_i^*)/2$

Above-gap $(|\varepsilon| < \Delta)$

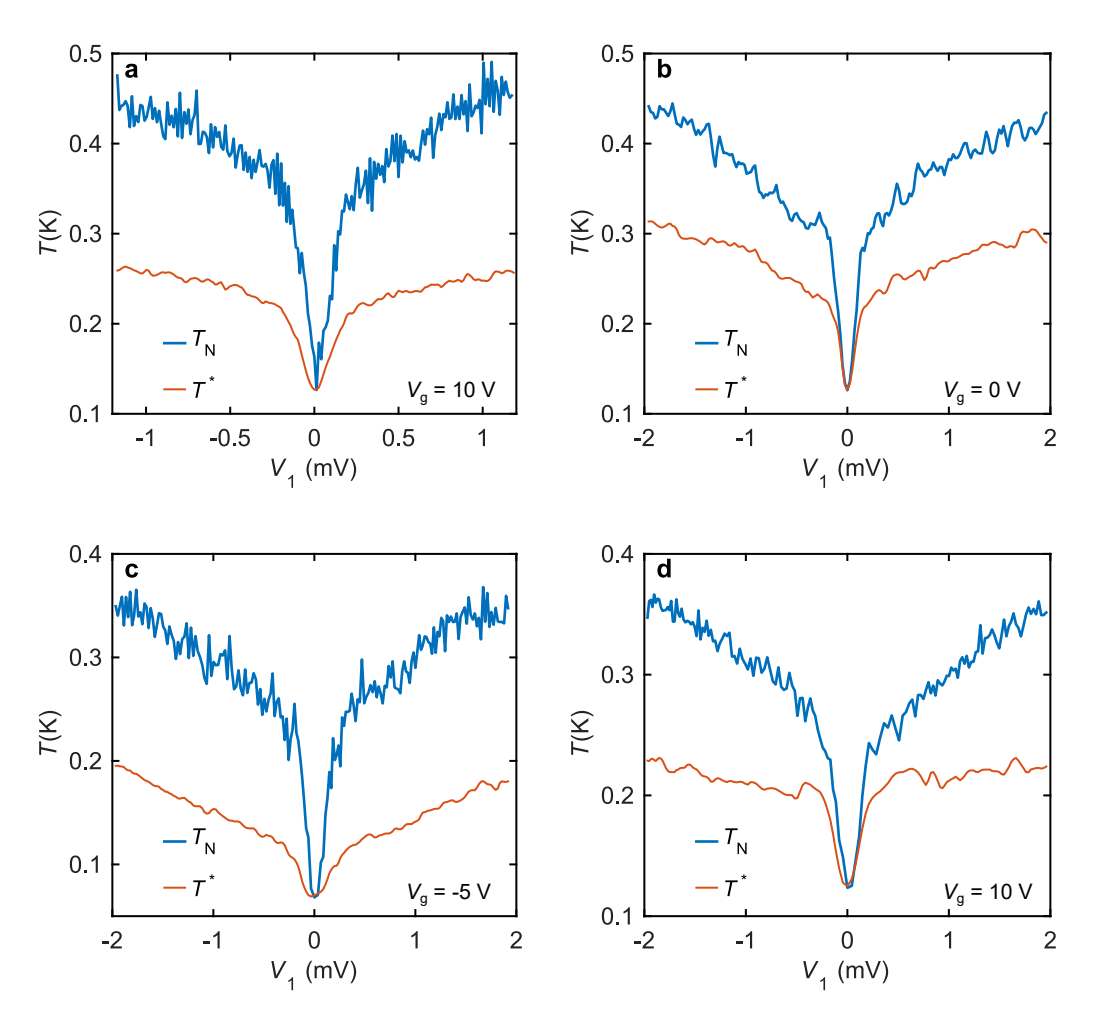
To calculate for energies above the superconducting gap, we need to take into account the fact that now there is a finite gradient of noise temperature near N/S interface. Then correction to T_N due to the finite r is of the first order and we can not neglect it. Fortunately, for energies above the gap, S terminal acts as regular normal lead, so we can assume $f^*(\varepsilon) = f_{1/2}^*(\varepsilon)$. In order to find $f^*(\varepsilon)$, one has to fulfill current conservation law for each energy:

$$G_2[f_2(\varepsilon) - f^*(\varepsilon)] + G_1[f_1(\varepsilon) - f^*(\varepsilon)] = r^{-1}[f^*(\varepsilon) - f_0(\varepsilon)]$$
(S9)

where $f_0(\varepsilon)$ is a Fermi-Dirac distribution in the normal state of grounded Al terminal and r is the interface resistance.

$$f^*(\varepsilon) = \frac{G_1 f_1(\varepsilon) + G_2 f_2(\varepsilon) + 1/r f_0(\varepsilon)}{G_1 + G_2 + r^{-1}}$$
(S10)

Noise vs. Resistive thermometry



Supplemental Material Fig. 12. (a) - (b) Measured noise and effective temperature of the floating NS junction (NSN - II device) at different back - gate voltages. Zero-bias thermometry underestimates noise one by the factor of ~ 2 .

Is this section we highlight the difference between noise thermometry and resistive thermometry approaches.

To describe numerically the resistive thermometry, we consider NS junction as a two-terminal coherent quasi-1D conductor with n channels and energy-dependent diagonal transmission coefficients $Tr_i(\varepsilon)$ connecting two reservoirs with temperatures $T_{\rm L}$ and $T_{\rm R}$. We now determine the linear response conductance G_1 in such a system, where a temperature bias across the conductor might be present.

If a small voltage bias dV is applied across the conductor, the linear-response current through the nanowire dI is [S2]:

$$dI = \frac{2e}{h} \sum_{i}^{n} \int Tr_{i}(\varepsilon) \left[f\left(\varepsilon - \frac{edV}{2}, T_{R}\right) - f\left(\varepsilon + \frac{edV}{2}, T_{L}\right) \right] d\varepsilon, \tag{S11}$$

where $f(\varepsilon, T)$ is the equilibrium Fermi-Dirac distribution at temperature T. We note, that the conductance temperature dependence in this model is fully enclosed in the energy dependence of $Tr_i(\varepsilon)$. Now we transform this equation by taking out the small bias from the distribution functions and separating the sum:

$$dI = \frac{2e}{h} \int \left[\sum_{i=1}^{n} Tr_{i}(\varepsilon) \right] \left[\frac{\partial f(\varepsilon, T_{R})}{\partial \varepsilon} \left(-\frac{edV}{2} \right) - \frac{\partial f(\varepsilon, T_{L})}{\partial \varepsilon} \left(\frac{edV}{2} \right) \right] d\varepsilon, \tag{S12}$$

which leads to the linear response conductance $G_{1,\text{non-eq}}$ in form:

$$G_{1} = \partial I/\partial V = -\frac{2e^{2}}{h} \frac{1}{2} \int \left[\sum_{i}^{n} Tr_{i}(\varepsilon) \right] \left[\frac{\partial f(\varepsilon, T_{R})}{\partial \varepsilon} + \frac{\partial f(\varepsilon, T_{L})}{\partial \varepsilon} \right] d\varepsilon = \frac{G_{1}(T_{R}) + G_{1}(T_{L})}{2}.$$
 (S13)

where $G_1(T)$ is the ordinary equilibrium conductance which can be measured by varying the bath temperature. The (S13) clearly demonstrates, that the temperature, measured via resistive thermometry T^* in the main text obeys a relation:

$$G_1(T^*) = \frac{G_1(T_{\rm R}) + G_1(T_{\rm L})}{2},$$
 (S14)

We note, that this result is only valid for the case of equilibrium distribution functions at both nanowire terminals. For the triple-step distribution expected for S terminal in our experiment, the conductance depends on the exact form of $Tr_i(\varepsilon)$.

We now compare this result for T^* with the expected noise temperature T_N when one terminal has significantly higher temperature $(T_R \gg T_L)$. For this case T_N can be expressed in form $T_N = \alpha T_R$, with coefficient α depending on the shape of distribution function at the terminal [S3]. For the double-step distribution $\alpha = 2/3$, while in the case of equilibrium distribution $\alpha = (1 + \ln(2))/2 \approx 0.56$.

Neglecting the non-linearity of of $G_1(T)$, which is present in experiment (see supplemental fig. 9b), we obtain that the relation $T_N \approx 4/3T^*$.

In experiment, however, the discrepancy between $T_{\rm N}$ and T^* is more prominent with $T_{\rm N}-T_{\rm bath}\approx 2(T^*-T_{\rm bath})$ (see supplemental fig. 12). Apart from the discussed earlier effect of the non-equilibrium distribution on G_1 , this inconsistency might be related to the dephasing being present in nanowire. Such dephasing may effectively break the nanowire into several coherent section, with possibly different signs of temperature dependence, leading to a further dampening of T^* compared to $T_{\rm N}$.

Non-local voltage generated by temperature bias

In order to describe the symmetric component of the non-local I-Vs presented in Fig. 4d of the main text we consider a thermoelectric generation of voltage. In the Landauer-Büttiker formalism, the conversion of the temperature bias to electric current is a result of the energy dependence of the eigen-channel transparencies $Tr_i(\varepsilon)$. Thermoelectric current generated in a short-circuited conductor can be written as:

$$I_{\text{TE}} = \frac{2e}{h} \sum_{i}^{n} \int Tr_{i}(\varepsilon) \left[f\left(\varepsilon, T_{\text{R}}\right) - f\left(\varepsilon, T_{\text{L}}\right) \right] d\varepsilon \approx \frac{2e}{h} \sum_{i}^{n} Tr'_{i} \int \varepsilon \left[f\left(\varepsilon, T_{\text{R}}\right) - f\left(\varepsilon, T_{\text{L}}\right) \right] d\varepsilon, \tag{S15}$$

where the quasiparticle energy ε is measured with respect to the chemical potential that is the same for the right and left leads of the conductor. Note that in this equation we approximated the energy dependence $Tr_i(\varepsilon)$ with the lowest order non-vanishing term $Tr_i(\varepsilon) = Tr_i(0) + Tr_i'\varepsilon$, where $Tr_i' \equiv dTr_i(\varepsilon)/d\varepsilon|_{\varepsilon=0}$. It is straightforward to see that eq. (S15) results in a parabolic T-dependence of I_{TE} :

$$I_{\rm TE} \approx \frac{\pi^2 k_B^2}{6} \frac{2e}{h} \sum_i^n Tr_i' \left[T_{\rm R}^2 - T_{\rm L}^2 \right].$$
 (S16)

Measured thermoelectric voltage that builds up on a floating conductor is simply $V_{\rm TE} = -I_{\rm TE}G_0^{-1}$, where $G_0 = 2e^2/h\sum_i^n Tr_i(0)$ is the linear-response conductance. For a small temperature difference $\Delta T \equiv T_{\rm R} - T_{\rm L} \ll T$, the eq. (S16) can be written as:

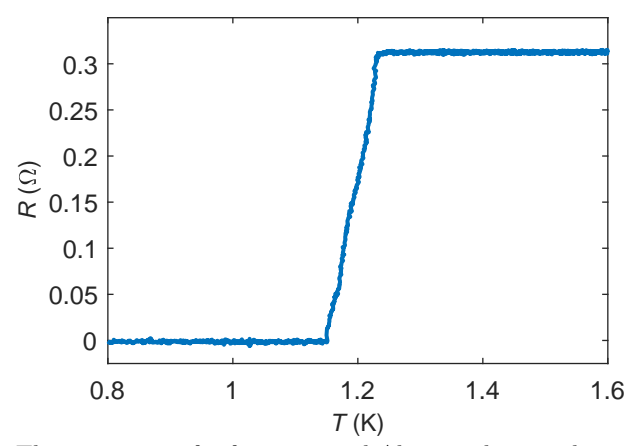
$$V_{\rm TE} \approx (S/T)T\Delta T$$
, where $S/T = -\frac{\pi^2 k_B^2}{3e} \sum_i^n Tr_i' \left[\sum_i^n Tr_i \right]^{-1}$. (S17)

In other words, in this approximation the thermoelectric response is fully characterized by the T-independent Seebeck parameter S/T. With this notation we obtain the expression for arbitrary thermal biases on the conductor:

$$V_{\rm TE} \approx (S/T) \frac{T_{\rm R}^2 - T_{\rm L}^2}{2},$$
 (S18)

that is used to fit the data for V_2^{symm} in Fig. 4d of the main text.

Critical Temperature of Al contacts



Supplemental Material Fig. 13. The resistance of a four-terminal Al strip, deposited via the same process, as the one used in the fabrication of the samples, featured in the main text.

The temperature dependence of superconducting Al, deposited via the same process as described in "Device Fabrication" was performed separately on the four-terminal Al strips, incorporated in the samples studied in [S4]. Here we present raw data (see Fig. 13), which leads to the estimate $T_c = 1.20 \pm 0.03 \,\mathrm{K}$, based on the position of the middle of transition.

Device fabrication

InAs nanowires grown by molecular beam epitaxy on Si substrate [S5] are ultrasonicated in isopropyl alcohol. Nanowires are drop casted on Si/SiO2 (300 nm) substrates [S6] with preliminary defined alignment marks. For superconducting contacts conventional electron beam lithography (EBL) followed by e-beam deposition of Al (150 nm) is utilized. To obtain the ohmic contacts, in-situ Ar ion milling is performed before Al deposition in a chamber with a base pressure below 10^{-7} mbar. Normal metal contacts are fabricated in two different ways (different device batches): magnetron sputtering or e-beam deposition. For sputtering (NS and NSN - I devices) in-situ Ar plasma etching is followed by sputtering of Ti/Au (5 nm/200 nm). Normal metal contacts Ti/Au (5 nm/150 nm) in device NSN - II are deposited in the same way as superconducting ones.

[[]S1] K. E. Nagaev and M. Büttiker, Phys. Rev. B 63, 081301 (2001).

[[]S2] Y. Blanter and M. Bttiker, Physics Reports 336, 1 (2000).

[[]S3] E. S. Tikhonov, D. V. Shovkun, D. Ercolani, F. Rossella, M. Rocci, L. Sorba, S. Roddaro, and V. S. Khrapai, Scientific Reports 6, 30621 EP (2016), article.

[[]S4] A. V. Bubis, A. O. Denisov, S. U. Piatrusha, I. E. Batov, V. S. Khrapai, J. Becker, J. Treu, D. Ruhstorfer, and G. Koblmller, Semiconductor Science and Technology **32**, 094007 (2017).

[[]S5] S. Hertenberger, D. Rudolph, M. Bichler, J. J. Finley, G. Abstreiter, and G. Koblmller, Journal of Applied Physics 108, 114316 (2010).

[[]S6] J. Becker, S. Morkötter, J. Treu, M. Sonner, M. Speckbacher, M. Döblinger, G. Abstreiter, J. J. Finley, and G. Koblmüller, Phys. Rev. B 97, 115306 (2018).